

Meson dynamics from locally exciting a particle-conserving Z_2 lattice gauge theory

Vaibhav Sharma* and Kaden R. A. Hazzard†

Department of Physics and Astronomy, Rice University, Houston, TX 77005 and

Smalley-Curl Institute, Rice University, Houston, TX 77005

(Dated: March 5, 2025)

Quantum simulation of lattice gauge theories is an important avenue to gain insights into both particle physics phenomena and constrained quantum many-body dynamics. There is a growing interest in probing analogs of high energy collision phenomena in lattice gauge theories that can be implemented on current quantum simulators. Motivated by this, we characterize the confined mesons that originate from a local high energy excitation in a particle-conserving 1D Z_2 lattice gauge theory. We focus on a simple, experimentally accessible setting that does not require preparation of colliding wavepackets and isolates the effects of gauge field confinement strength and initial state energy on the nature of propagating excitations. We find that the dynamics is characterized by the propagation of a superposition of differently sized mesons. The linear confinement leads to meson size oscillations in time. The average meson size and oscillation frequency are controlled by the strength of the gauge field confinement. At a constant confinement field, the average meson length is controlled by the initial excitation's energy. Higher energies produce longer mesons and their effective mass depends strongly on their size: longer mesons propagate more slowly out of the central excitation. Mesons of different sizes get spatially filtered with time due to different speeds. We show that this phenomenology is a consequence of linear confinement and remains valid in both the strong and weak confinement limit. We present simple explanations of these phenomena supported by exact numerics.

I. INTRODUCTION

Gauge theories model vast phenomena, ranging from the interactions of fundamental particles to the collective behaviour of spins in condensed matter systems [1]. Over the past decades, we have learnt a great deal about gauge theories like QED and QCD through large-scale particle collider experiments where high-energy particles are smashed together. These high energies can give rise to new particles and interesting non-equilibrium phenomena such as a quark-gluon plasma and short-lived bound states [2]. However, it is computationally challenging to access the real-time non-equilibrium phenomena in these collisions experiments using quantum Monte Carlo lattice QCD techniques on classical computers.

Quantum computers and quantum simulators can bridge this gap. By implementing these gauge theories on a discrete lattice, quantum computers can exactly simulate real-time quantum dynamics of high-energy phenomena in a table-top experiment. In recent years, there has been considerable progress in quantum simulation experiments of some simple models such as Z_2 and $U(1)$ lattice gauge theories [3–14].

Although these simple models are far from the more complicated $SU(3)$ QCD in three dimensions, they display some of the features we expect in QCD such as linear confinement of particles, pair production, and string breaking [12, 15–17]. Thus studying such simple models already can give us insights into the dynamical phenomena we expect in gauge theories. It also gives us a

roadmap where we can leverage current quantum simulator technology to understand simple lattice gauge theory models and gradually build-up towards a full simulation of gauge theories like QCD. In addition to the connection to high energy physics, these gauge theory models also emerge as descriptions of low energy phases in condensed matter systems such as topologically ordered quantum spin liquids [18–23]. The interplay of gauge symmetry and strong interactions also leads to a rich set of quantum many-body phenomena [24–30]. In the condensed matter context, it is important to note that these theories genuinely live on a lattice, as opposed to the lattice being introduced to approximate continuous space, leading to unique phenomena.

The study of dynamical phenomena in lattice gauge theories is attracting considerable attention in recent years. These gauge theories show exotic non-ergodic phenomena such as lack of thermalization due to confinement and Hilbert-space fragmentation [8, 31–34], quantum many-body scars [35–39] and Floquet time crystals [40]. Analogs of QCD phenomena such as confinement dynamics [13, 14, 41, 42], pair production through string breaking [12, 15–17, 43–47], false vacuum decay [48], and dynamical hadron formation [49, 50] have been found in theoretical calculations and some quantum simulator experiments.

These successes have opened up an exciting new avenue of probing analogs of high energy particle collision phenomena within these simple lattice gauge theories. Some recent works have studied schemes to prepare moving wavepackets for collisions [51, 52] and numerically analyzed scattering processes [49, 53–55]. In these studies, the dynamics involves a rich interplay of multiple kinds of bound excitations, resonant processes of particle pair production and string fluctuation dynamics.

* vaibhavsharma@rice.edu

† kaden@rice.edu

This rich complexity can mask the fundamental role played solely by gauge-mediated interactions. For instance, in the absence of resonant string breaking and particle production processes, it is not fully clear how the nature of the propagating bound state excitations systematically varies with the strength of the confining field and the magnitude of a localized energy injection event. Through this work, we intend to understand such building blocks of collision phenomena in lattice gauge theories in a simpler experimentally accessible setting and probe the effects of confinement strength and initial energy.

In our work, we characterize the nature of propagating excitations that emerge from a localized high energy excitation in a particle-conserving 1D Z_2 lattice gauge theory model. A schematic of the scenario we study is shown in Fig. 1(a) in which a high energy excitation disperses into outward propagating bound mesons. In a collider experiment, such a high energy region occurs at the location of a collision. However in a controlled quantum simulation, a high energy excitation region can also be created without a collision. We consider starting with product states where a small local region is excited to a tunable higher energy using local gauge spin rotations as opposed to collisions of moving wavepackets. Our setting provides an alternate scenario of creating non-equilibrium excitations from an initial energy injection.

In particular, we analyze the excitations produced by initially localizing two particles in the center of a 1D chain in its vacuum state. Our model conserves particle number and shows confinement of two particles into mesons of different possible lengths [56]. We use a mix of simple analytical calculations and exact diagonalization numerics to characterize the structure of mesons and their propagation speed as they emerge from this excited region.

We find that the long time state is characterized by propagation of a superposition of differently sized mesons, with the average size inversely dependent on the confinement field. The meson size oscillates in time and the oscillations get larger as the confinement field reduces. These larger mesons slowly propagate out, damping out the oscillations near the center. Some of this phenomenology is similar to what has been seen in wavepacket scattering studies in lattice gauge theories where a particle-anti particle pair after a collision continues to periodically move apart and come back for another collision [51, 55]. The scaling of the average meson size and the oscillation frequency are qualitatively described by analytical results obtained from an associated Wannier-Stark problem, which becomes exact as we approach infinitely large confinement field strengths.

We also consider the effect of tuning the initial state energy at a fixed confinement field. The average length of mesons that propagate monotonically increases as a function of initial state energy, instead of the spatial size of the initial excitation. As the meson size increases, its propagation speed is slower, which slows down the spread of particle density away from the excitation region. Due

to this differential in meson speed, the mesons separate out spatially according to their size as a function of time. This is a consequence of linear confinement and we find that this feature holds true even for cases where the confining field is weaker than the particle hopping term. We show that for weaker confining fields, mesons longer than a certain size experience a slow down.

II. MODEL

We consider hard-core bosons occupying the sites of a one-dimensional lattice, coupled to spin-1/2 degrees of freedom on the links of the lattice. The 1D Z_2 lattice gauge theory Hamiltonian we study is

$$H = -J \sum_i (b_{i+1}^\dagger \sigma_{i,i+1}^x b_i + h.c.) + h \sum_i \sigma_{i,i+1}^z. \quad (1)$$

The operators b, b^\dagger annihilate and create hardcore bosons on site i and σ^x, σ^z are spin-1/2 Pauli operators for the link degrees of freedom. The bosons are considered as the matter particles while the spin-1/2 particles on the links are considered to be the gauge fields. A basis state of the model is shown in Fig. 1(b).

Bosons hop between nearest-neighbor sites by flipping a link spin. This is the Z_2 analog of minimal coupling that couples the matter's kinetic energy to the gauge field vector potential. In this analogy, $\sigma_{i,i+1}^x = e^{iA_{i,i+1}}$ where $A_{i,i+1} = \pi/2(\sigma_{i,i+1}^x - 1)$. The electric field operator conjugate to the vector potential operator $A_{i,i+1}$ is given by $\sigma_{i,i+1}^z$. Thus the field term proportional to $h\sigma_{i,i+1}^z$ is the energy cost of the electric field due to excitations of the gauge field.

The model in Eq. 1 describes a Z_2 gauge theory since the Hamiltonian is invariant under a local Z_2 gauge transformation generated by the operator, $G_i = \sigma_{i-1,i}^z (-1)^{n_i} \sigma_{i,i+1}^z$. Here $n_i = b_i^\dagger b_i$ denotes the number of bosons on site i . Under G_i , the operators in the Hamiltonian undergo Z_2 transformations, $G_i b_i G_i^\dagger = e^{i\pi} b_i$, $G_i b_i^\dagger G_i^\dagger = e^{-i\pi} b_i^\dagger$ and $G_i \sigma_{i,i+1}^x G_i^\dagger = e^{i\pi} \sigma_{i,i+1}^x$.

There is a local conservation law at each site since $[G_i, H] = 0$. The Hamiltonian eigenstates can thus be chosen to also be the eigenstates of the operator G_i at each site. The eigenvalues of G_i are ± 1 . Different choices of the G_i eigenvalues correspond to independent and physically distinct sectors of the Hamiltonian's Hilbert space [24]. Throughout this work, we only consider states $|\psi\rangle$ where $G_i |\psi\rangle = +1 |\psi\rangle$ for all sites i . This constraint implies that $\sigma_{i-1,i}^z (-1)^{n_i} \sigma_{i,i+1}^z |\psi\rangle = |\psi\rangle$. We can rewrite it as, $\sigma_{i-1,i}^z \sigma_{i,i+1}^z |\psi\rangle = e^{i\pi/2(\sigma_{i-1,i}^z - \sigma_{i,i+1}^z)} = (-1)^{n_i} |\psi\rangle$. This can be interpreted as a Gauss law where the local matter density determines the electric field configuration around it.

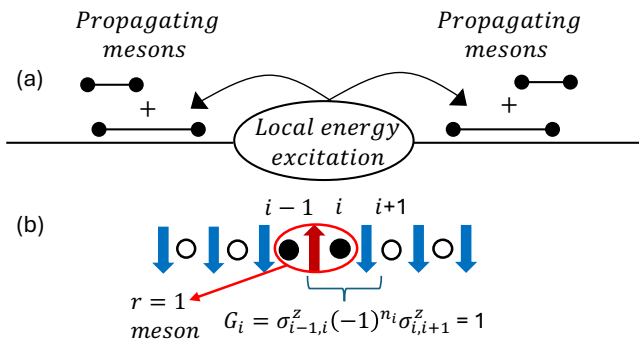


FIG. 1. (a) Dynamics of mesons: Mesons propagate out of the localized energy excitation in both directions in a 1D chain governed by a Z_2 lattice gauge theory. The state is described by a superposition of different meson sizes. The confinement field and the initial excitation energy determine the meson size distribution. The propagation speed varies with the meson size. (b) A basis state of the 1D Z_2 lattice gauge model. Open and filled circles represent absence and presence of a boson on sites labeled by index i . The red and blue arrows are link gauge spins representing $\sigma^z = \pm 1$ respectively. The quantity, $G_i = \sigma_{i-1,i}^z (-1)^{n_i} \sigma_{i,i+1}^z = 1$ is conserved on each site. The red ellipse denotes a meson where the two bosons are next to each other, called an $r = 1$ meson.

III. THE TWO-PARTICLE SECTOR

The Hamiltonian in Eq. 1 conserves total boson number. In this work, we consider dynamics when there are only two bosons present in the system. We consider configurations where the two bosons are added onto the vacuum, the particle-free ground state. The vacuum state has all the gauge spins aligned along the negative z -axis ($\sigma_{i,i+1}^z = -1$) to minimize the electric field energy (we assume $h > 0$). An example of such a two-particle configuration is shown in Fig. 1(b). Due to the Gauss law constraint on each site, the link spin configuration can be completely determined by the position of the bosons. We thus get, $\sigma_{i,i+1}^z = \prod_{j \leq i} (-1)^{n_j}$. The states in the two-boson sector can be characterized by the position indices of the two bosons, i_1 and i_2 . The link spins between sites i_1 and i_2 are the only ones aligned in the positive z -direction leading to an electric field energy cost of $+2h$ for each such link. This is what leads to confinement of particles into mesons in this model.

Using the two bosons' positions (i_1, i_2) to label the basis states, we can write down the Hamiltonian in Eq. 1 in the two-boson sector as

$$H = -J \sum_{i_1, i_2} (|i_1 + 1, i_2\rangle \langle i_1, i_2| + |i_1, i_2 + 1\rangle \langle i_1, i_2| + \text{h.c.}) + 2h \sum_{i_1, i_2} |i_1 - i_2\rangle |i_1, i_2\rangle \langle i_1, i_2|. \quad (2)$$

We use the center-of-mass ($c = (i_1 + i_2)/2$) and relative ($r = i_1 - i_2$) coordinates to further simplify the

Hamiltonian. The Hamiltonian in Eq. 2 becomes

$$H = -J \sum_c \sum_{r=1}^{\infty} (|c + 1/2\rangle \langle c| + \text{h.c.}) (|r + 1\rangle \langle r| + \text{h.c.}) + 2h \sum_{r=1}^{\infty} r |r\rangle \langle r| \quad (3)$$

Here the center of mass coordinate c can take half-integer and integer values while the relative coordinate r only takes integer values. The relative coordinate has a linear potential term in Eq. 3. In the ground state, at any finite h/J , two particles are confined by this potential into mesons [56]. The center-of-mass coordinate is free and thus the mesons can delocalize. In this work, we study the two-particle sector dynamics in terms of the center-of-mass and relative coordinates. The different relative coordinate values correspond to different types of possible meson excitations. The smallest possible meson is the $r = 1$ meson where the two bosons are right next to each other. In later sections, we calculate how the size of the propagating mesons depends on field term h/J and the energy of the initial local excitation. We will also determine how meson size affects its propagation speed.

A. Diagonalizing the Hamiltonian

We can diagonalize the Hamiltonian in Eq. 3 by considering the eigenstates to be of the form, $|\psi_{n,k}\rangle = \Phi_k \otimes \Gamma_n = (\sum_c \phi_c^k |c\rangle) \otimes (\sum_r \gamma_r^n |r\rangle)$ that satisfy the equation, $H|\psi_{n,k}\rangle = E_{n,k}|\psi_{n,k}\rangle$. Note that the center-of-mass states only have a hopping term in the Hamiltonian. Thus plane wave states of the form, $\phi_c^k = e^{ikc}/\sqrt{2L-1}$ are eigenstates for the center-of-mass degree of freedom. Here L is the total number of sites in the chain. Due to the half integer steps of the coordinate c , the momentum k ranges from $-\pi$ to π in steps of $2\pi/(2L-1)$. We can find the function γ_r^n by substituting ϕ_c^k into the eigenvalue equation of the Hamiltonian in Eq. 3 and projecting it onto $|c\rangle \otimes |r\rangle$. We then get

$$E_{n,k} \gamma_r^n = -2J \cos(k/2) (\gamma_{r+1}^n + \gamma_{r-1}^n) + 2hr \gamma_r^n. \quad (4)$$

Note that the relative coordinate is restricted to $r \geq 1$. Without such a restriction, this describes a Wannier-Stark ladder and Eq. 4 admits Bessel function solutions where $\gamma_r^n = J_{r-n}(2J \cos(k/2)/h)$ [57]. The energy eigenvalue in that case is given by, $E_{n,k} = 2hn$ where n is integer quantized. The energy is independent of the center-of-mass momentum leading to a large degeneracy. However in our case, $r \leq 0$ is not allowed and thus we must enforce the boundary condition that $\gamma_{r=0}^n = 0$. This is akin to adding an infinite potential wall at $r = 0$. As a result, the eigenstates are no longer Bessel functions. The exact eigenstates are given by Lommel polynomials and the eigenenergies are obtained from the zeros of the Lommel polynomial [58].

Even with this boundary condition, the eigensolutions are analytically rather simple in the large- h/J and small- h/J limit. These limits essentially capture a complete picture of the physics. We now derive the solution in these two simple limits.

1. Large- h/J limit

When $h/J \gg 1$, the Bessel function solutions seen earlier approach the exact eigenstates. At large h/J , the asymptotic form of the solutions is, $J_{r-n} \sim (2J \cos(k/2)/h)^{|r-n|}$. The amplitude at $r = 0$ is $\sim (2J \cos(k/2)/h)^{-|n|}$. As $h/J \rightarrow \infty$, when $n \geq 1$, this amplitude goes to zero, satisfying the boundary condition in the asymptotic limit. The energy eigenvalues are quantized in this limit and given by, $E_{n,k} = 2hn$. The n^{th} eigenstate is sharply peaked around $r = n$ with power law tails $(1/h^{|r-n|})$. Seen another way, the zeroth order $h/J \rightarrow \infty$ solution has the n^{th} eigenstate as a delta function on $r = n$ with the eigenenergy $2hn$ where $n \geq 1$. The hopping term proportional to J in Eq. 4 provides first order perturbation to the wavefunction and gives it a tail such that the amplitude on level $r \neq n$ is $(2J \cos(k/2)/h)^{|r-n|}$.

2. Small- h/J limit

When $|h/J| \ll 1$, we can take a continuum limit of the eigenvalue problem in Eq. 4 to get

$$E_{n,k} \gamma_r^n = -2J \cos(k/2) \frac{d^2 \gamma_r^n}{dr^2} + 2hr \gamma_r^n \quad (5)$$

We define $r' = l_0 r$ where $l_0 = (J \cos(k/2)/h)^{1/3}$ and rewrite Eq. 5 as

$$-\frac{d^2 \gamma_r^n}{dr'^2} + (r' - E'_{n,k}) \gamma_r^n = 0 \quad (6)$$

with $E'_{n,k} = E_{n,k}/2(Jh^2 \cos(k/2))^{1/3}$. Eq. 6 is solved by Airy functions of the first kind. Thus $\gamma_r^n = \text{Ai}(r' - E'_{n,k})$. The Airy functions decay exponentially to zero as $r' \rightarrow \infty$. The boundary condition at $r = 0$ implies that, $\gamma_0^n = \text{Ai}(-E'_{n,k}) = 0$. The scaled eigenenergy $E'_{n,k}$ is determined by the location of the n^{th} zero of the Airy function. The eigenenergy becomes, $E_{n,k} = -2z_n(Jh^2 \cos(k/2))^{1/3}$, where z_n is the location of the n^{th} zero; these zeros are $z_1 = -2.33811, z_2 = -4.08795, z_3 = -5.52056$ and so on. Note that in this small h/J limit, the eigenenergies do depend on the center-of-mass momentum and have a non-linear dependence on the confining field h .

At intermediate values of the confining field h/J , the exact eigenfunctions are given by Lommel polynomials [58]. We will later see that even for h/J as small as

~ 1 , the functional form of quantities such as average meson size and size oscillation frequencies can be extracted from the large- h/J limit solutions.

IV. EFFECT OF CONFINEMENT FIELD ON MESON DYNAMICS

In this section, we characterize the meson dynamics from simple initial states as a function of confinement field strength. We first consider the initial excitation where an $r = 1$ meson is localized at the center of a 1D chain of length L . This corresponds to the initial configuration shown in Fig. 1(b). In the $|r, c\rangle$ (relative and center-of-mass coordinate) basis, the wavefunction at time $t = 0$ is given by $|\psi(0)\rangle = |1, (L+1)/2\rangle$. Under the Hamiltonian in Eq. 3, the system wavefunction evolves in time and can be written as, $|\psi(t)\rangle = \sum_{c,r} g_{c,r}(t) |c, r\rangle$. In our calculations, we fix $L = 100$ and use exact diagonalization to calculate the time-evolved wavefunctions.

We show the dynamics of propagating excitations in Fig. 2 at two values of the confining field, $h = 1.1J$ and $h = 0.3J$. In Fig. 2(i),(ii), particles delocalize through light-cone like structures emanating from the central excitation region at time $t = 0$. The outermost cones in both cases represent fast moving excitations. The inner cone has a slower spread and has substructures that show diamond shaped particle tracks that also slowly spread out from the center. These are more pronounced and wider for smaller $h = 0.3J$. These tracks show similarities to the ones found after wavepacket collisions in Ref. [51, 55] where they were interpreted as the two particles coming together and colliding multiple times. We will show in later sections that we can interpret them as meson size oscillations which gradually spread out from the center as these mesons delocalize. In Fig. 2(iii),(iv), we can clearly see that at a given time, smaller mesons occupy the largest center-of-mass positions away from the central excitation region. This suggests that meson size is inversely related to propagation speed. Due to different speed, mesons of different sizes get spatially filtered in time evolution. We will show that this is a consequence of the linear confinement of mesons and persists for both $h > J$ and $h < J$ regimes.

We use the system wavefunction at long times to characterize the propagating excitations. In particular, we calculate the average meson size, $r_{\text{avg}}(t) = \sum_r r |\langle r | \psi(t) \rangle|^2$ as a function of time. The meson excitations propagate equally in both the directions away from the center. We determine the speed at which the mesons propagate by calculating the temporal slope of the center-of-mass coordinate's standard deviation, c_s , defined as

$$c_s(t)^2 = \sum_c c^2 |\langle c | \psi(t) \rangle|^2 - \left(\sum_c c |\langle c | \psi(t) \rangle|^2 \right)^2 \quad (7)$$

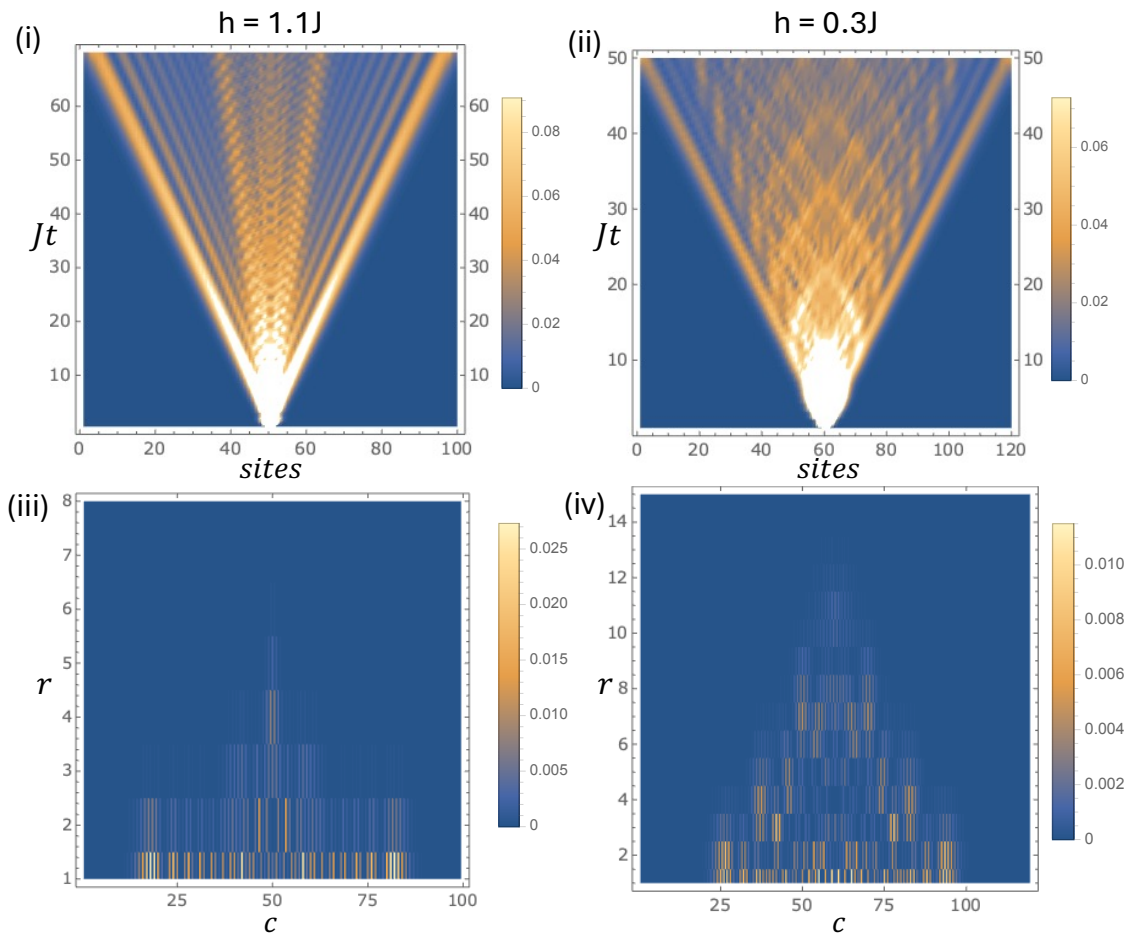


FIG. 2. (i),(ii): Particle density as a function of site index (x-axis) and time, Jt (y-axis) for (i) $h/J = 1.1$ and (ii) $h/J = 0.3$. With time, the mesons delocalize in light-cones like structures. The outermost cones represent faster moving excitations. The slower moving inner cones show substructures with diamond shaped particle tracks denoting temporal oscillation of meson size. (iii),(iv): Snapshot of occupation probability as a function of meson size (r) and its center-of-mass position (c) at (iii) $Jt = 50$ for $h = 1.1J$ and (iv) $Jt = 30$ for $h = 0.3J$. In both cases, smaller sized mesons delocalize the farthest, suggesting larger mesons propagate slower. The different speeds lead to a spatial filtering of meson sizes as larger mesons have more probability of being detected closer to the center during time evolution.

At time $t = 0$, the average center-of-mass coordinate is at $(L + 1)/2$ with $c_s = 0$. As the mesons propagate in both directions, the center-of-mass coordinate's distribution widens around the initial state average. The width is characterized by c_s and is expected to increase as a function of time. Its slope gives the speed of propagation of excitations.

In Fig. 3(a),(b), we show r_{avg} and c_s respectively as a function of time for a typical case when $h = 1.1J$. After some transient behavior, r_{avg} settles and oscillates around a steady value of $r'_{\text{avg}} = 1.46$. This suggests that the propagating excitations are a superposition of different meson sizes. We also see that r_{avg} oscillates in time, suggesting meson size oscillations. The width of center-of-mass distribution c_s steadily increases from $c_s = 0$ as the mesons propagate outwards from the center. This is expected since the confined mesons can freely delocalize. The average size of propagating mesons and frequency of

size oscillations are strongly dependent on the confining field, h/J .

In Fig. 4, we plot r'_{avg} as a function of the confinement field h/J . This is the value around which r_{avg} oscillates in time. We find that as h/J decreases, the propagating meson excitations get longer such that $r'_{\text{avg}} - 1 \propto 1/h$. We also extract the frequency of oscillations of r_{avg} at long time. We take the Fourier transform of the r_{avg} vs time data at long times and use the frequency of the dominant peak as the oscillation frequency. Fig. 4 shows this frequency of oscillations, ω as a function of h/J . We find that $\omega \propto h$ for large h/J and deviates for smaller h/J .

These features can be qualitatively understood from Eq. 4 where the relative coordinate (meson size) moves in a Wannier-Stark ladder of a linearly tilted potential. For moderate values of h/J , the relative coordinate can take values away from the boundary ($r = 1$) and the

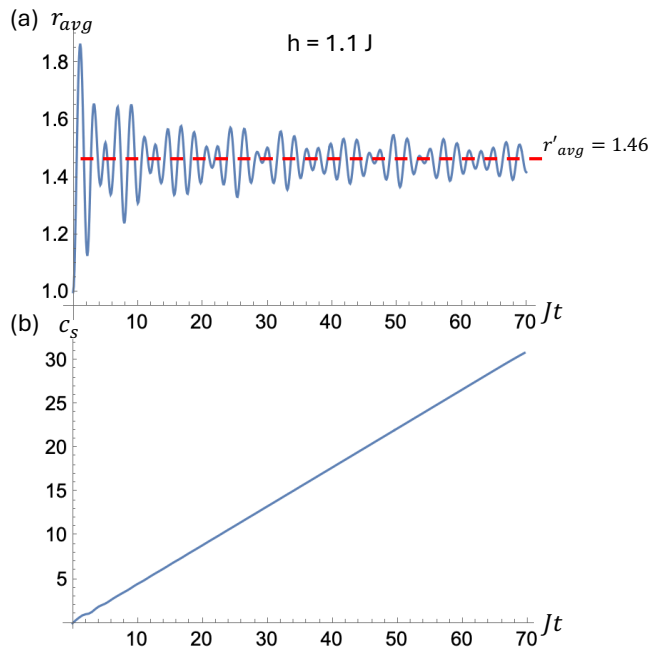


FIG. 3. Dynamics after initializing an $r = 1$ meson at the center of a chain of $L = 100$ sites for $h = 1.1J$. (a) Average size of propagating mesons, r_{avg} , vs time, t . The meson size oscillates in time about a value of $r'_{\text{avg}} = 1.46$. (b) Width, c_s , of the center-of-mass distribution vs time, t . Due to propagating mesons, the width of the center-of-mass distribution increases monotonically with time.

energy is nearly quantized, independent of the center-of-mass momentum. In this scenario, the relative coordinate undergoes breathing oscillations around its initial value. These breathing oscillations quantify the spread in meson size as a function of time. In Appendix A 1, we show that the breathing oscillation function is given by, $r_s = \sqrt{2}J/h|\sin(ht)|$. The oscillation frequency of this breathing is given by, $\omega = 2h$ showing the $\omega \propto h$ dependence. The amplitude of r_s sets the spread of meson sizes and controls the inverse h/J scaling of the average meson size, r'_{avg} . For smaller h/J , the meson size oscillations become larger and higher length mesons obtain finite probability of occupation, as can be seen in Fig. 2(ii),(iv).

When $h/J \gg 1$, the relative coordinate is restricted to values around $r = 1$. The mean value of the relative coordinate oscillates as a function of time. In Appendix A 2, we show $r_{\text{avg}} = 1 + J^2/(2h^2) + J^2 \sin^2(ht)/(2h^2)$. We again get frequency of oscillations, $\omega = 2h$ but the spread of average meson size around its initial value ($r = 1$) scales as $(h/J)^{-2}$. We note that the $(h/J)^{-1}$ dependence of r'_{avg} (seen in Fig. 4) only captures an overall trend for moderate to large values of h/J . For very large values of h/J , the curve is expected to follow an $(h/J)^{-2}$ dependence.

When $h/J \ll 1$, the eigenfunctions are better described by Airy functions where the energy is a non-linear

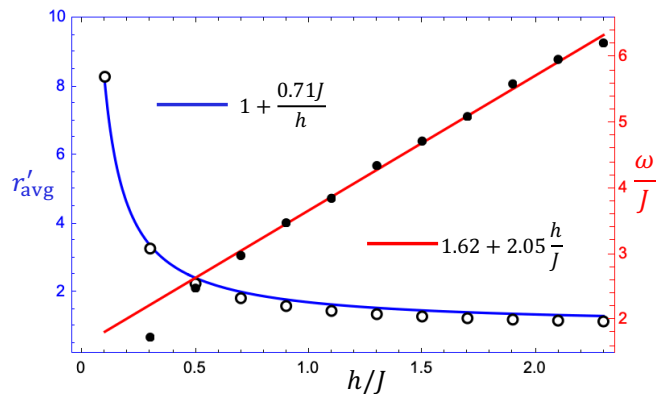


FIG. 4. Long-time average size of propagating mesons, r'_{avg} , vs confinement field, h/J shown by open markers. The solid blue line is a fit to a function, $r'_{\text{avg}} - 1 \propto 1/h$. Frequency of oscillations, ω of average meson size, r_{avg} vs field h/J shown by solid black dots. The solid red line is a fit of ω as a linear function of h .



FIG. 5. A central excitation in a superposition of an $r = 1$ and $r = 2$ meson, tuned by the angle θ of one of the gauge spins. The gray circles show a finite probability between 0 and 1 of having a particle controlled by θ . The excitation energy is, $E(\theta) = \sin \theta + 2h \sin^2(\theta/2) + 2h$.

function of both the center-of-mass momentum and h/J (see Sec. III A). In terms of the field dependence, we expect the frequency ω to scale as $(h/J)^{2/3}$ and r'_{avg} to scale as $(h/J)^{-1/3}$. Due to the special boundary condition of the relative coordinate, scalings can be more easily predicted compared to prefactors.

V. EFFECT OF THE INITIAL STATE'S ENERGY ON MESON DYNAMICS

At fixed values of the confining field h/J , we can tune the nature of excitations that emerge by changing the initial excitation energy. This is akin to collider experiments where changing the center-of-mass collision energy determines what excitations can be produced. We consider adding some amplitude of $r = 2$ meson to the $r = 1$ meson initial state in order to tune the energy as shown in Fig. 5. Such a configuration corresponds to tilting one of the gauge spins by an angle θ about the y -axis. In the $|r, c\rangle$ basis, such initial states are

$$|\psi_\theta(0)\rangle = \cos \frac{\theta}{2} |1, (L+1)/2\rangle - \sin \frac{\theta}{2} |2, L/2+1\rangle. \quad (8)$$

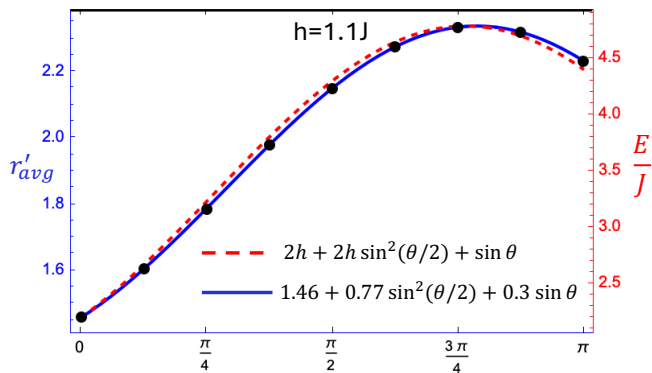


FIG. 6. At $h = 1.1J$, initial state's energy, E (red dashed line) and average meson size, r'_{avg} (black dots are data and blue solid line is a fit) as a function of θ . The meson size and energy have the same functional dependence on θ . Higher energy leads to longer meson excitations that propagate.

Using the Hamiltonian in Eq. 3, the energy of this initial state is, $E(\theta) = \sin \theta + 2h \sin^2(\theta/2) + 2h$. The term $2h \sin^2(\theta/2)$ comes from the confining electric field energy of the $r = 2$ meson amplitude and the $\sin \theta$ term denotes the kinetic energy from the hopping term of the Hamiltonian. We tune θ from 0 to π , varying the initial state from an $r = 1$ meson continuously to an $r = 2$ meson. The energy, $E(\theta)$, varies non-monotonically with θ as shown in Fig. 6. This is due to the kinetic energy contribution. Starting from $|\psi_\theta(0)\rangle$ at a fixed confining field, $h = 1.1J$, we calculate the average size, r'_{avg} , of propagating mesons at long times and plot it in Fig. 6 as a function of θ . We find that r'_{avg} closely tracks the initial state's energy, having the same functional dependence on θ as energy does. If the initial energy increases, r'_{avg} rises, indicating larger mesons. Note that although the initial state is spatially largest when $\theta = \pi$ (an $r = 2$ meson), the average size of mesons is lower compared to the case when $\theta = 3\pi/4$ where the initial energy is higher. This occurs because the initial kinetic energy also gets converted into the size of mesons.

This can be understood from the nature of the eigenstate solutions of the Hamiltonian in Eq. 3 that we saw in Sec III in the large h/J limit. The eigenenergy given by $E_{n,k} = 2hn$ is independent of the center-of-mass momentum k . For large h/J , each eigenfunction corresponding to $E_{n,k}$ is sharply peaked around the relative coordinate value of $r = n$, denoting an $r = n$ meson. Therefore even though the Hamiltonian has contributions from both the hopping term (kinetic energy) and meson confinement terms (electric field energy), the eigenenergies only depend on the length of the meson excitation. This property persists even for cases where $h/J < 1$. We have numerically checked that the eigenenergies of the Hamiltonian in Eq. 4 are quantized in the bulk of the spectrum (where states with $r \gg 1$ contribute more) for h/J as low as 0.1. The quantization gets destroyed for small h/J as we near the bottom of the spectrum where $r \sim 1$ states

contribute significantly. However, a higher initial energy can place the system closer to the bulk of the spectrum for small h/J , somewhat counteracting this lack of quantization.

The speed of the propagating mesons is strongly affected by their size at a fixed confining field, h/J . We show the particle density evolution as a function of time for different initial energies and correspondingly different average meson sizes in Fig. 7. We can clearly see that as the average meson size increases, the particle density spread becomes narrower, indicating that longer mesons are propagating at slower speeds. In Fig. 8, we plot the speed of the propagating meson excitations as a function of their size, r'_{avg} , at $h = 1.1J$ and $h = 0.3J$ by changing the initial state energy as discussed above. The speed is calculated by finding the slope, $v = dc_s/d(Jt)$ at long times from the c_s vs Jt graph (example shown in Fig. 3(b)). We find that meson size and speed are inversely related in both strong confinement ($h > J$) and weak confinement ($h < J$) cases. Longer mesons propagate more slowly. Thus a detector placed far away from the center would detect smaller mesons first and would have to wait for a longer time to detect larger mesons. This dependence of meson speed on meson size is due to the kinetic constraints arising from the linear confining potential. Following arguments similar to those in [42, 53] we show how linear confinement leads to faster speeds for shorter mesons in the $h/J \gg 1$ limit. Furthermore we argue how this phenomenology remains valid in our scenario even when $h < J$.

We first show how an $r = 1$ meson would move faster than an $r = 2$ meson and so on for longer mesons when $h > J$. Consider an $r = 1$ meson at some large value of h/J . The entire meson can hop to its right only by a second order hopping process as shown in Fig. 9(a). This process changes its center-of-mass position by 1 but leaves the relative coordinate unchanged. By second order perturbation theory, the matrix element for this process is given by $-J^2/2h$. As the confining field h/J increases, the $r = 1$ mesons propagate slower.

Now let's consider an $r = 2$ meson. In a similar vein, we can consider processes which lead to the meson hopping to its right. There are two possibilities at second order. The first is shown in Fig. 9(b) where the right particle hops to the right first and then the left particle follows. The matrix element for this process is $-J^2/2h$ similar to the $r = 1$ meson. The second possibility shown in Fig. 9(c) is similar, but here the left particle hops first, followed by the right particle. The matrix element of this process is $J^2/2h$. The matrix elements of these two processes are equal and opposite in sign. They cancel out and thus the $r = 2$ meson cannot hop by a second order hopping process. The leading order process that can cause motion is fourth order, shown in Fig. 9(d). Here the right particle hops two sites and then the left particle follows. The center of mass changes by 2 and the matrix element for this process is $-J^4/16h^3$. The propagation speed for an $r = 2$ meson would be $v \sim J^4/8h^3$ as op-

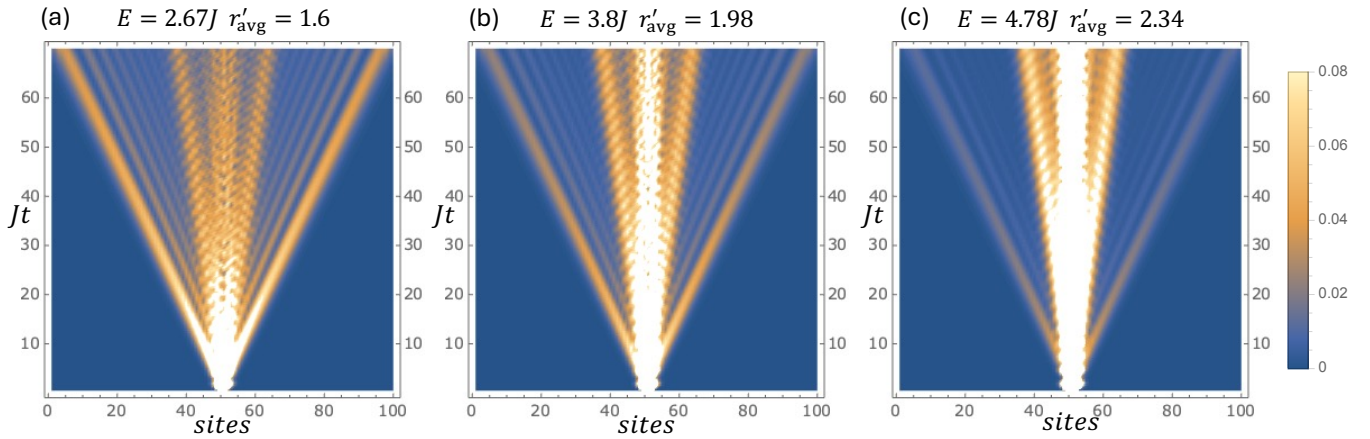


FIG. 7. Particle density on each site (x-axis) as a function of time, Jt (y-axis), for $h = 1.1J$ for different initial energies, E , and average meson size, r'_{avg} . (a) $E = 2.67J$ and $r'_{\text{avg}} = 1.6$, (b) $E = 3.8J$ and $r'_{\text{avg}} = 1.98$ and (c) $E = 4.78J$ and $r'_{\text{avg}} = 2.34$. We can see that as the average meson size, r'_{avg} , increases with energy, the particle density spread becomes narrower. Longer mesons are propagating at slower speeds away from the center.

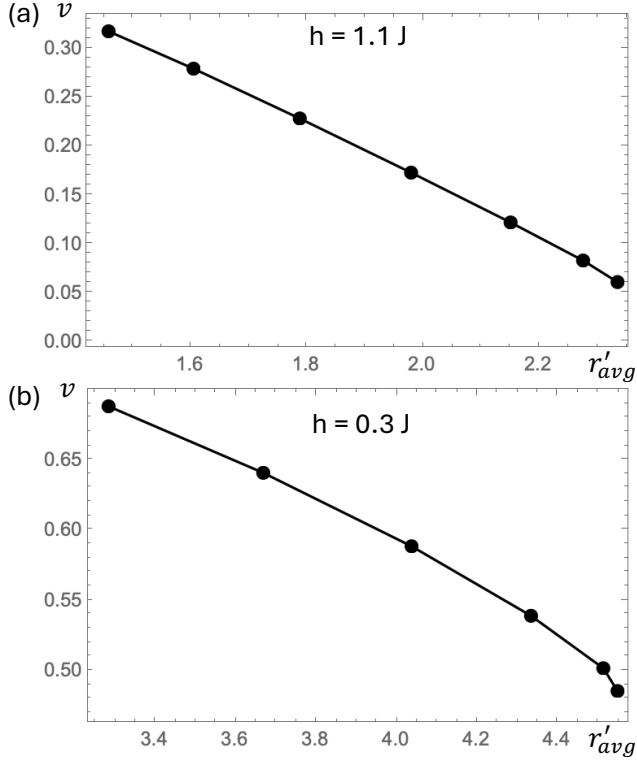


FIG. 8. The speed of propagating mesons, v , as a function of average meson size, r'_{avg} , at (a) $h = 1.1J$ and (b) $h = 0.3J$. The meson size at a fixed h is varied by varying the initial energy of the state. The speed v and r'_{avg} are inversely related, making longer mesons slower. This suggests that longer mesons are effectively heavier due to the Z_2 gauge constraint. This is not only true when $h > J$ but persists for values where $h < J$.

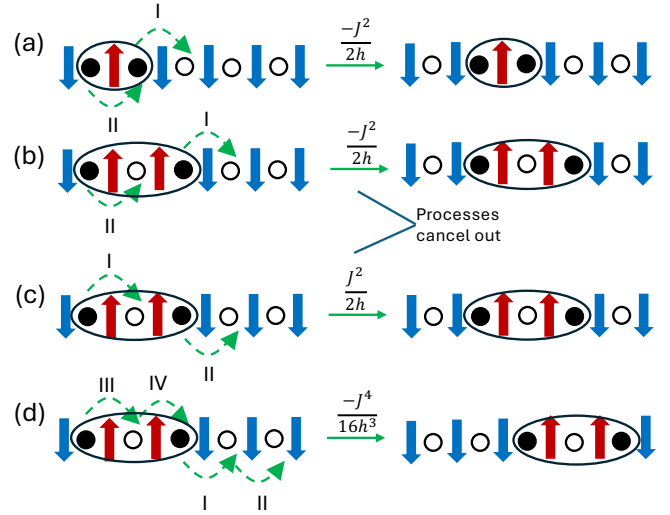


FIG. 9. (a) Second-order hopping process (path I followed by path II) of an $r = 1$ meson with matrix element $-1/(2h)$. (b),(c) Two possible second order hopping processes of an $r = 2$ meson with path I followed by path II and vice versa. The matrix elements for the two processes are equal and opposite and hence cancel. (d) A fourth order hopping process ($I \rightarrow II \rightarrow III \rightarrow IV$) with matrix element $-1/16h^3$ that changes the center of mass position of an $r = 2$ meson by 2.

posed to $J^2/2h$ for an $r = 1$ meson. At large values of h/J , the $r = 2$ meson would be much slower than the $r = 1$ meson. Using a similar argument, one can show that an $r = 3$ meson can only propagate by a sixth order process and is even slower than $r = 2$ mesons.

The previous argument seems to hold only when $h/J > 1$. However, we will now show that the general argument survives even when $h/J < 1$, as seen by slower propagating longer mesons in Fig. 8(b). Due to the sign cancel-

lations caused by linear confinement, a meson of length n needs at least a $2n^{\text{th}}$ order hopping process to move. The matrix element for such a process, H_{2n} , is given by

$$H_{2n} = -\frac{J^{2n}}{2h \cdot 4h \cdots 2nh \cdots 4h \cdot 2h} \quad (9)$$

$$= J \left(\frac{J}{2h} \right)^{2n-1} \frac{n}{(n!)^2} \quad (10)$$

We show the matrix element, H_{2n} , for $h/J = 0.1, 0.3, 0.5$ and 1.1 as a function of n in Fig. 10. We can see that for all values of h/J shown here, the matrix element is peaked at some finite $n = n_p$ and larger values of $n > n_p$ ultimately contribute exponentially smaller matrix elements. This is due to the growing $(n!)^2$ factor coming from linear confinement. For mesons shorter than n_p , the leading order matrix element is not the largest. Contributions from several possible beyond leading order processes makes the relation of speed and size more complicated. But for mesons longer than n_p , an increase in meson size corresponds to a successively lower matrix element even in the leading order process. Thus increase in length would correspond to a decrease in speed.

In Fig. 8, the average meson sizes are greater than the corresponding peak n_p in Fig. 10(a),(c) and thus speed decreases as meson size increases due to increase in energy. We can estimate how the peak n_p varies as a function of h/J . Using Stirling's formula for large n , we can write, $H_{2n} \sim e^{2n(\ln|J/h| - \ln n)}$. This function is peaked at $n_p = J/(he)$ where e is the base of the natural logarithm. As h/J decreases, n_p increases and the peak broadens. The mesons that propagate slower thus become progressively longer as we approach the continuum limit. The longer mesons slowly propagate out of the central excitation region and damp out the size oscillations at the center as seen prominently in Fig. 2(ii).

VI. PROPOSED EXPERIMENTAL IMPLEMENTATION USING A SPIN MODEL

Lattice gauge theories have seen recent implementations in quantum simulator platforms such as cold atoms [3, 5, 8], superconducting qubit-based quantum computer platforms [4, 7, 9, 11, 14], and trapped ions [12, 13]. A promising avenue to implement our particle-conserving Z_2 lattice gauge theory model is by simulating a pure spin model on a quantum computer. The spin model is obtained from the Hamiltonian in Eq. 1 by eliminating the matter fields using the gauge constraint. As shown in [24, 25], the Hamiltonian maps onto a pure spin model of the form

$$H = -\sum_i \frac{(1 - \sigma_{i-1,i}^z \sigma_{i+1,i+2}^z)}{2} \sigma_{i,i+1}^x + h \sum_i \sigma_{i,i+1}^z \quad (11)$$

In the particle vacuum, all the spins point down. A particle excitation corresponds to a domain wall in the

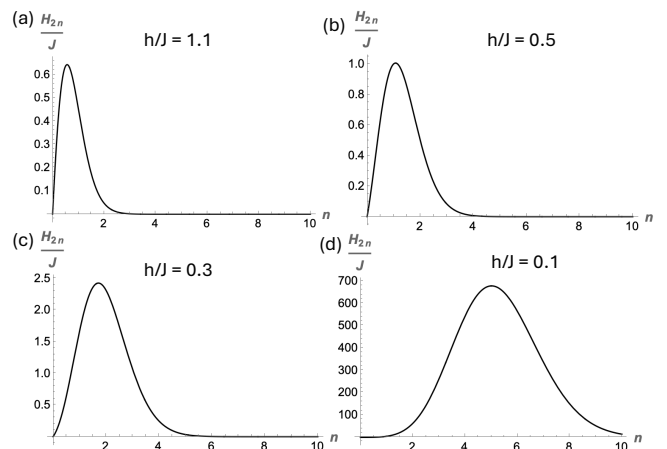


FIG. 10. Leading order matrix element, H_{2n} that causes motion of a length n meson by n sites for (a) $h/J = 1.1$, (b) $h/J = 0.5$, (c) $h/J = 0.3$ and (d) $h/J = 0.1$. For mesons of length beyond the peak n , meson length is inversely related to propagation speed since the leading order matrix elements start becoming smaller with size. As h/J decreases, the peak broadens and moves to larger n , making the slowdown apparent for only very long mesons.

spins. The first term in the spin model encodes particle hopping from an occupied site (presence of a spin domain wall) to an empty site (absence of a domain wall) by flipping the link spin in the path. The initial state in the dynamics considered here are simply product states of the spins. The initial spin configuration for the $r = 1$ meson initial state is shown in Fig. 1(b). When we tune the initial state energy by introducing a finite amplitude of $r = 2$ meson, we simply need to prepare the spin configuration shown in Fig. 5. Here the central spin is pointing up and the spin next to it is rotated along the y -axis by an angle θ using a single qubit y -rotation.

For studying dynamics, the spin model in Eq. 11 can be Trotterized on a quantum computer. The only non-traditional part of this model is the three-spin term encoding particle hopping. It requires a native three qubit gate or its decomposition into a set of two-qubit gates. All the quantities discussed in our work can be accessed by analyzing the snapshots obtained by measuring all the spins at any time step. A particular snapshot would contain two spin domain walls, indicating the two particles. The distance between the domain walls averaged over snapshots gives the average meson size, r_{avg} . The center-of-mass distribution's width, c_s can also be found by recording the position of domain walls that occur at any time step in the system.

VII. SUMMARY AND OUTLOOK

We studied the confined mesons that propagate from a localized high energy excitation in a 1D particle-conserving Z_2 lattice gauge theory. We considered simple

local excitations by adding two matter particles on the gauge field vacuum state and using single spin rotations to tune the energy of the initial excitation. Our scheme provides an alternative to scenarios involving preparation of colliding wavepackets and isolates the effect of confinement field strength and energy of the initial excitation on the nature of propagating excitations.

We performed exact diagonalization numerics to simulate the dynamics and found that the long-time state is characterized by the propagation of a superposition of different sizes of mesons. The mesons show size oscillations in time. The average meson size depends inversely on the confinement field while the frequency of oscillations is proportional to the confining field. The meson size oscillations become larger as the confinement field strength decreases. These size oscillations are similar to the particle tracks seen after wavepacket collisions in lattice gauge theories [51, 55]. We were able to explain these behaviors analytically by solving an associated Wannier-Stark problem in the large field (h/J) limit.

We also found that as we increase the energy of the initial local excitation, the average meson size monotonically increases, independent of the spatial extent of the initial state. Both the kinetic energy and confinement energy contribution of the initial state gets reflected into the meson size.

We calculated the speed of the meson propagation as a function of their size and found that longer mesons are effectively heavier and propagate more slowly. Longer mesons carry higher gauge field energy excitations giving them a larger effective mass. Due to different propagation speeds, mesons of different sizes spatially get separated as we evolve in time. We found that these results hold not only when h/J is large but also for smaller values of h/J . We showed that for any finite linear confining potential, the leading order meson hopping matrix elements show exponential decay for mesons beyond a certain length. This threshold length rises as the confinement field becomes weaker and continues all the way until we approach a continuum limit. Throughout the study, we only consider simple initial states that create a localized high energy excitation region, making these phenomena experimentally accessible in the near-term quantum simulators.

Although the model studied here is a simple one-dimensional lattice gauge theory, we already see some features that are reminiscent of standard gauge theories. This includes real-time oscillations of particle flavor (meson size oscillations) and effective mass of particles governed by the gauge field excitations they carry. In particular, these features appear even when the confinement field strength is moderate to small and do not require any string breaking or particle pair production processes. The nature of excitations can be tuned by either varying the confinement field strength or the initial state energy, giving us an intuitive way of probing lattice gauge theories on quantum simulators.

It would be interesting to explore whether these fea-

tures occur in generic linear confining gauge theories in an arbitrary dimension or if they are just a special case of one dimensional gauge theories. An interesting direction is to study higher dimensional analogs of the problem we studied and the effects of introducing particle non-conserving terms. We can expect to see richer phenomenology even in this simple set-up as longer mesons can either break up into shorter mesons or create other kinds of gauge field excitations such as magnetic field like excitations.

VIII. ACKNOWLEDGMENTS

VS acknowledges support from the J. Evans Attwell-Welch fellowship by the Rice Smalley-Curl Institute. KRAH acknowledges support from the W. M. Keck Foundation (Grant No. 995764), the National Science Foundation (PHY-1848304), and the Office of Naval Research (N00014-20-1-2695). We thank Sayak Guha Roy and Andrew Long for fruitful discussions.

Appendix A: Meson size breathing oscillation function

Here we analytically calculate the dynamics of the relative coordinate r as a function of time in the large h/J limit. Earlier we showed that the system eigenstates in the large- h/J and high excitation limit are given by $|\psi_{n,k}\rangle = \sum_{c,r} \phi_c^k \gamma_r^n |c, r\rangle$ where $\phi_c^k = e^{ikc}/\sqrt{2L-1}$ and $\gamma_r^n = J_{r-n}(2J \cos(k/2)/h)$. These functions are peaked around $r = n$ with tails decaying as $(2J \cos(k/2)/h)^{|r-n|}$. The eigenenergy $E_{n,k} = 2hn$ is independent of k .

For simplicity, we project into a fixed center-of-mass momentum k state, say $k = 0$ and then consider the dynamics of the relative coordinate, r starting from some initial value of r_0 . We expand the $h = \infty$ eigenfunction $|r_0\rangle$ to first order in J/h to get

$$|\tilde{r}_0\rangle = |r_0\rangle - \frac{J}{2h}|r_0+1\rangle + \frac{J}{2h}|r_0-1\rangle. \quad (\text{A1})$$

The eigenenergy of this state is $2hr_0$. We consider an initial state $|\psi(0)\rangle = |r_0\rangle$. We can expand this in terms of the eigenstates $|\tilde{r}\rangle$ to first order in J/h as

$$|\psi(0)\rangle = |r_0\rangle = |\tilde{r}_0\rangle - \frac{J}{2h}|\tilde{r}_0-1\rangle + \frac{J}{2h}|\tilde{r}_0+1\rangle. \quad (\text{A2})$$

At time t , the state evolves under the Hamiltonian given in the eigenvalue problem in Eq. 4. Up to a global

phase factor, it becomes

$$\begin{aligned}
|\psi(t)\rangle &= |\tilde{r}_0\rangle - \frac{J e^{2iht}}{2h} |\tilde{r}_0 - 1\rangle + \frac{J e^{-2iht}}{2h} |\tilde{r}_0 + 1\rangle \\
&= \left(1 + \frac{J^2 \cos(2ht)}{2h^2}\right) |r_0\rangle + \frac{J}{2h} (1 - e^{2iht}) |r_0 - 1\rangle \\
&\quad - \frac{J}{2h} (1 - e^{-2iht}) |r_0 + 1\rangle. \quad (\text{A3})
\end{aligned}$$

1. When $r_0 > 1$

We can analytically calculate the spread of relative coordinate, r , about r_0 as a function of time by calculating $r_s^2 = \langle (r - r_0)^2 \rangle - \langle (r - r_0) \rangle^2$. Up to leading order, we find that $\langle r \rangle \sim r_0$ and $\langle (r - r_0)^2 \rangle \sim 2 \sin^2(ht) J^2 / h^2$. Thus

we get the breathing function, $r_s = \sqrt{2} J / h |\sin ht|$. The amplitude of this function sets the meson size spread and captures the $(h/J)^{-1}$ dependence of r'_{avg} with oscillation frequency, $\omega = 2h$.

2. When $r_0 = 1$

Due to the boundary condition, we are restricted to $r \geq 1$. Thus we drop any terms of the form $|r_0 - 1\rangle$ from the first line of Eq. A3. We can again calculate the average relative coordinate value $\langle r \rangle$ and find that $\langle r \rangle = 1 + J^2 / (2h^2) + J^2 \sin^2(ht) / (2h^2)$. This shows that r_{avg} oscillates with a frequency, $\omega = 2h$. We also get an $(h/J)^{-2}$ dependence of r'_{avg} .

-
- [1] J. B. Kogut, An introduction to lattice gauge theory and spin systems, *Rev. Mod. Phys.* **51**, 659 (1979).
- [2] I. Arsene *et al.*, Quark–gluon plasma and color glass condensate at RHIC? the perspective from the BRAHMS experiment, *Nuclear Physics A* **757**, 1–27 (2005).
- [3] B. Yang, H. Sun, R. Ott, H.-Y. Wang, T. V. Zache, J. C. Halimeh, Z.-S. Yuan, P. Hauke, and J.-W. Pan, Observation of gauge invariance in a 71-site Bose–Hubbard quantum simulator, *Nature* **587**, 392 (2020).
- [4] Z. Wang, Z.-Y. Ge, Z. Xiang, X. Song, R.-Z. Huang, P. Song, X.-Y. Guo, L. Su, K. Xu, D. Zheng, and H. Fan, Observation of emergent \mathbb{Z}_2 gauge invariance in a superconducting circuit, *Phys. Rev. Res.* **4**, L022060 (2022).
- [5] C. Schweizer, F. Grusdt, M. Berngruber, L. Barbiero, E. Demler, N. Goldman, I. Bloch, and M. Aidelsburger, Floquet approach to \mathbb{Z}_2 lattice gauge theories with ultracold atoms in optical lattices., *Nature Physics* **15**, 1168 (2019).
- [6] M. Aidelsburger *et al.*, Cold atoms meet lattice gauge theory, *Philosophical Transactions of the Royal Society A* **380** (2022).
- [7] J. Mildenerger, W. Mruczkiewicz, J. C. Halimeh, Z. Jiang, and P. Hauke, Probing confinement in a \mathbb{Z}_2 lattice gauge theory on a quantum computer, (2022), arXiv:2203.08905 [quant-ph].
- [8] Z.-Y. Zhou, G.-X. Su, J. C. Halimeh, R. Ott, H. Sun, P. Hauke, B. Yang, Z.-S. Yuan, J. Berges, and J.-W. Pan, Thermalization dynamics of a gauge theory on a quantum simulator, *Science* **377**, 311 (2022).
- [9] G. Gyawali, *et al.*, Observation of disorder-free localization and efficient disorder averaging on a quantum processor, (2024), arXiv:2410.06557 [quant-ph].
- [10] C. W. Bauer *et al.*, Quantum simulation for high-energy physics, *PRX Quantum* **4**, 027001 (2023).
- [11] Z. Wang, Z.-Y. Ge, Z. Xiang, X. Song, R.-Z. Huang, P. Song, X.-Y. Guo, L. Su, K. Xu, D. Zheng, and H. Fan, Observation of emergent F_2 gauge invariance in a superconducting circuit, *Phys. Rev. Res.* **4**, L022060 (2022).
- [12] A. De, A. Lerosé, D. Luo, F. M. Surace, A. Schuckert, E. R. Bennewitz, B. Ware, W. Morong, K. S. Collins, Z. Davoudi, A. V. Gorshkov, O. Katz, and C. Monroe, Observation of string-breaking dynamics in a quantum simulator (2024), arXiv:2410.13815 [quant-ph].
- [13] W. L. Tan, P. Becker, F. Liu, G. Pagano, K. S. Collins, A. De, L. Feng, H. B. Kaplan, A. Kyprianidis, R. Lundgren, W. Morong, S. Whitsitt, A. V. Gorshkov, and C. Monroe, Domain-wall confinement and dynamics in a quantum simulator, *Nature Physics* **17**, 742–747 (2021).
- [14] E. A. Martinez, C. A. Muschik, P. Schindler, D. Nigg, A. Erhard, M. Heyl, P. Hauke, M. Dalmonte, T. Monz, P. Zoller, and R. Blatt, Real-time dynamics of lattice gauge theories with a few-qubit quantum computer, *Nature* **534**, 516–519 (2016).
- [15] U. Borla, J. J. Osborne, S. Moroz, and J. C. Halimeh, String breaking in a 2 + 1d \mathbb{Z}_2 lattice gauge theory, (2025), arXiv:2501.17929 [quant-ph].
- [16] T. A. Cochran *et al.*, Visualizing dynamics of charges and strings in (2+1)d lattice gauge theories, (2024), arXiv:2409.17142 [quant-ph].
- [17] T. Pichler, M. Dalmonte, E. Rico, P. Zoller, and S. Montangero, Real-time dynamics in U(1) lattice gauge theories with tensor networks, *Phys. Rev. X* **6**, 011023 (2016).
- [18] A. Celi, B. Vermersch, O. Viyuela, H. Pichler, M. D. Lukin, and P. Zoller, Emerging two-dimensional gauge theories in Rydberg configurable arrays, *Phys. Rev. X* **10**, 021057 (2020).
- [19] R. Nath, M. Dalmonte, A. W. Glaetzle, P. Zoller, F. Schmidt-Kaler, and R. Gerritsma, Hexagonal plaquette spin–spin interactions and quantum magnetism in a two-dimensional ion crystal, *New Journal of Physics* **17**, 065018 (2015).
- [20] J. Shah, G. Nambiar, A. V. Gorshkov, and V. Galitski, Quantum spin ice in three-dimensional Rydberg atom arrays, (2024), arXiv:2301.04657 [cond-mat.quant-gas].
- [21] F. Grusdt and L. Pollet, \mathbb{Z}_2 parton phases in the mixed-dimensional $t - J_z$ model, *Phys. Rev. Lett.* **125**, 256401 (2020).
- [22] D. González-Cuadra, L. Tagliacozzo, M. Lewenstein, and A. Bermudez, Robust topological order in fermionic \mathbb{Z}_2 gauge theories: From Aharonov-Bohm instability to soliton-induced deconfinement, *Phys. Rev. X* **10**, 041007 (2020).
- [23] R. Samajdar, D. G. Joshi, Y. Teng, and S. Sachdev, Emergent \mathbb{Z}_2 gauge theories and topological excitations

- in Rydberg atom arrays, *Phys. Rev. Lett.* **130**, 043601 (2023).
- [24] V. Sharma and E. J. Mueller, One-dimensional Z_2 lattice gauge theory in periodic Gauss-law sectors, *Phys. Rev. A* **110**, 033314 (2024).
- [25] M. Kebrić, L. Barbiero, C. Reinmoser, U. Schollwöck, and F. Grusdt, Confinement and Mott transitions of dynamical charges in one-dimensional lattice gauge theories, *Phys. Rev. Lett.* **127**, 167203 (2021).
- [26] T. Chanda, D. González-Cuadra, M. Lewenstein, L. Tagliacozzo, and J. Zakrzewski, Devil's staircase of topological Peierls insulators and Peierls supersolids, *SciPost Phys.* **12**, 076 (2022).
- [27] M. Kebrić, U. Borla, U. Schollwöck, S. Moroz, L. Barbiero, and F. Grusdt, Confinement induced frustration in a one-dimensional lattice gauge theory, *New Journal of Physics* **25**, 013035 (2023).
- [28] A. Smith, J. Knolle, R. Moessner, and D. L. Kovrizhin, Dynamical localization in Z_2 lattice gauge theories, *Phys. Rev. B* **97**, 245137 (2018).
- [29] A. Smith, J. Knolle, D. L. Kovrizhin, and R. Moessner, Disorder-free localization, *Phys. Rev. Lett.* **118**, 266601 (2017).
- [30] M. Brenes, M. Dalmonte, M. Heyl, and A. Scardicchio, Many-body localization dynamics from gauge invariance, *Phys. Rev. Lett.* **120**, 030601 (2018).
- [31] A. N. Ciavarella, C. W. Bauer, and J. C. Halimeh, Generic Hilbert space fragmentation in Kogut–Susskind lattice gauge theories, (2025), arXiv:2502.03533 [quant-ph].
- [32] J.-Y. Desaulles, G.-X. Su, I. P. McCulloch, B. Yang, Z. Papić, and J. C. Halimeh, Ergodicity breaking under confinement in cold-atom quantum simulators, *Quantum* **8**, 1274 (2024).
- [33] Z.-C. Yang, F. Liu, A. V. Gorshkov, and T. Iadecola, Hilbert-space fragmentation from strict confinement, *Phys. Rev. Lett.* **124**, 207602 (2020).
- [34] T. Chanda, J. Zakrzewski, M. Lewenstein, and L. Tagliacozzo, Confinement and lack of thermalization after quenches in the Bosonic Schwinger model, *Phys. Rev. Lett.* **124**, 180602 (2020).
- [35] G. Calajò, G. Cataldi, M. Rigobello, D. Wanisch, G. Magnifico, P. Silvi, S. Montangero, and J. C. Halimeh, Quantum many-body scarring in a non-abelian lattice gauge theory, (2025), arXiv:2405.13112 [cond-mat.quant-gas].
- [36] J. Osborne, I. P. McCulloch, and J. C. Halimeh, Quantum many-body scarring in $2 + 1d$ gauge theories with dynamical matter, (2024), arXiv:2403.08858 [cond-mat.quant-gas].
- [37] J. C. Halimeh, L. Barbiero, P. Hauke, F. Grusdt, and A. Bohrdt, Robust quantum many-body scars in lattice gauge theories, *Quantum* **7**, 1004 (2023).
- [38] B. Andrade, U. Bhattacharya, R. W. Chhajlany, T. Graß, and M. Lewenstein, Observing quantum many-body scars in random quantum circuits, *Phys. Rev. A* **109**, 052602 (2024).
- [39] A. S. Aramthottil, U. Bhattacharya, D. González-Cuadra, M. Lewenstein, L. Barbiero, and J. Zakrzewski, Scar states in deconfined Z_2 lattice gauge theories, *Phys. Rev. B* **106**, L041101 (2022).
- [40] A. Russomanno, S. Notarnicola, F. M. Surace, R. Fazio, M. Dalmonte, and M. Heyl, Homogeneous Floquet time crystal protected by gauge invariance, *Phys. Rev. Res.* **2**, 012003 (2020).
- [41] M. Kormos, M. Collura, G. Takács, and P. Calabrese, Real-time confinement following a quantum quench to a non-integrable model, *Nature Physics* **13**, 246–249 (2016).
- [42] S. Pai and M. Pretko, Fractons from confinement in one dimension, *Phys. Rev. Res.* **2**, 013094 (2020).
- [43] G. Magnifico, M. Dalmonte, P. Facchi, S. Pascazio, F. V. Pepe, and E. Ercolessi, Real time dynamics and confinement in the z_n Schwinger-Weyl lattice model for $1+1$ QED, *Quantum* **4**, 281 (2020).
- [44] F. M. Surace, P. P. Mazza, G. Giudici, A. Leroze, A. Gambassi, and M. Dalmonte, Lattice gauge theories and string dynamics in Rydberg atom quantum simulators, *Phys. Rev. X* **10**, 021041 (2020).
- [45] J.-Y. Desaulles, T. Iadecola, and J. C. Halimeh, Mass-assisted local deconfinement in a confined Z_2 lattice gauge theory, (2024), arXiv:2404.11645 [cond-mat.quant-gas].
- [46] R. Verdel, F. Liu, S. Whitsitt, A. V. Gorshkov, and M. Heyl, Real-time dynamics of string breaking in quantum spin chains, *Phys. Rev. B* **102**, 014308 (2020).
- [47] R. Verdel, G.-Y. Zhu, and M. Heyl, Dynamical localization transition of string breaking in quantum spin chains, *Phys. Rev. Lett.* **131**, 230402 (2023).
- [48] Z.-H. Zhu, Y. Liu, G. Lagnese, F. M. Surace, W.-Y. Zhang, M.-G. He, J. C. Halimeh, M. Dalmonte, S. C. Morampudi, F. Wilczek, Z.-S. Yuan, and J.-W. Pan, Probing false vacuum decay on a cold-atom gauge-theory quantum simulator, (2024), arXiv:2411.12565 [cond-mat.quant-gas].
- [49] J. Vovrosh, R. Mukherjee, A. Bastianello, and J. Knolle, Dynamical hadron formation in long-range interacting quantum spin chains, *PRX Quantum* **3**, 040309 (2022).
- [50] Z. Wang, F. Wang, J. Vovrosh, J. Knolle, F. Mintert, and R. Mukherjee, Quantum simulation of hadronic states with Rydberg-dressed atoms, *Phys. Rev. A* **109**, 032613 (2024).
- [51] G.-X. Su, J. Osborne, and J. C. Halimeh, A cold-atom particle collider, (2024), arXiv:2401.05489 [cond-mat.quant-gas].
- [52] Z. Davoudi, C.-C. Hsieh, and S. V. Kadam, Scattering wave packets of hadrons in gauge theories: Preparation on a quantum computer, *Quantum* **8**, 1520 (2024).
- [53] F. M. Surace and A. Leroze, Scattering of mesons in quantum simulators, *New Journal of Physics* **23**, 062001 (2021).
- [54] E. R. Bennewitz, B. Ware, A. Schuckert, A. Leroze, F. M. Surace, R. Belyansky, W. Morong, D. Luo, A. De, K. S. Collins, O. Katz, C. Monroe, Z. Davoudi, and A. V. Gorshkov, Simulating meson scattering on spin quantum simulators, (2024), arXiv:2403.07061 [quant-ph].
- [55] R. Belyansky, S. Whitsitt, N. Mueller, A. Fahimniya, E. R. Bennewitz, Z. Davoudi, and A. V. Gorshkov, High-energy collision of quarks and mesons in the Schwinger model: From tensor networks to circuit QED, *Phys. Rev. Lett.* **132**, 091903 (2024).
- [56] U. Borla, R. Verresen, F. Grusdt, and S. Moroz, Confined phases of one-dimensional spinless fermions coupled to Z_2 gauge theory, *Phys. Rev. Lett.* **124**, 120503 (2020).
- [57] D. Emin and C. F. Hart, Existence of Wannier-Stark localization, *Phys. Rev. B* **36**, 7353 (1987).
- [58] G. C. Stey and G. Gusman, Wannier-Stark ladders and the energy spectrum of an electron in a finite one dimen-

sional crystal, *Journal of Physics C: Solid State Physics*
6, 650–656 (1973).